



# A Hierarchical Bayesian Framework for Stellar Obliquity Distribution Inference

JIAYIN DONG <sup>1,\*</sup> DAN FOREMAN-MACKEY <sup>1</sup> AND ET AL.

<sup>1</sup>Center for Computational Astrophysics, Flatiron Institute, 162 Fifth Avenue, New York, NY 10010, USA

(Received; Revised; Accepted)

Submitted to the AAS Journals

## ABSTRACT

Stellar obliquity  $\psi$ , the angle between a planet’s orbital axis and its host star’s spin axis, traces the formation and evolution of a planetary system. In transiting-exoplanet observations, only the sky-projected stellar obliquity  $\lambda$  can be measured. To determine the true stellar obliquity  $\psi$ , information on the stellar inclination  $i_*$  is also needed. Here we find that while the stellar inclination is crucial for understanding the obliquity of individual systems, it is not a requirement for determining the population-level stellar obliquity. The constraints on the stellar obliquity distribution are mainly driven by the sky-projected stellar obliquities. We introduce a flexible, hierarchical Bayesian framework that can infer the stellar obliquity distribution solely from sky-projected stellar obliquities. Stellar inclination measurements are optional input in the model, and if not available, they are assumed to be isotropically distributed. When applying the framework to all exoplanetary systems with sky-projected stellar obliquity measurements, we find that the stellar obliquity distribution is unimodal and peaked at zero degrees. Misaligned systems have nearly isotropic stellar obliquities, which could have important implications for the formation and evolution of close-in planets.

## 1. INTRODUCTION

Stellar obliquity  $\psi$  describes the angle between a planet’s orbital axis  $\mathbf{n}_{\text{orb}}$  and its host star’s spin axis  $\mathbf{n}_*$ . This angle is an important tracer of a planetary system’s formation environment and dynamical evolution. The evolution of stellar obliquity can be roughly broken down into three stages. First, the formation and evolution of a protoplanetary disk determine the primordial stellar obliquity (e.g., Bate et al. 2010; Lai et al. 2011; Batygin 2012). Second, post-formation dynamical evolution in the planetary system, such as planet-planet scattering (e.g., Rasio & Ford 1996; Chatterjee et al. 2008; Nagasawa et al. 2008; Beaugé & Nesvorný 2012), von Zeipel-Kozai-Lidov mechanisms (e.g., Wu & Murray 2003; Naoz 2016), and secular chaos (Wu & Lithwick 2011), can excite the mutual inclinations between planetary or stellar companions and alter the stellar obliquity. Lastly, the tidal force can reduce the stellar obliquity by realigning the host star’s spin axis with the planet’s or-

bitual axis, if the tidal dissipation in the star is efficient (e.g., Winn et al. 2010; Albrecht et al. 2012). Additionally, massive stars with convective cores could generate internal gravity waves and dissipate angular momentum to their radiative zones, potentially affecting the stellar obliquity (Rogers et al. 2012, 2013).

It is yet unclear if all of these physical and dynamic processes apply to exoplanetary systems. These proposed mechanisms have different predictions on stellar obliquity distributions (see Albrecht et al. 2022, and references therein). For example, the secular chaos mechanism suggests that the stellar obliquity would never exceed 90° (e.g., Teyssandier et al. 2019). The stellar Kozai mechanism predicts that the stellar obliquity distribution should be bimodal and concentrated at 40° and 140° (e.g., Fabrycky & Tremaine 2007; Anderson et al. 2016; Vick et al. 2019). The multiple-planet scattering mechanism proposes that the majority of systems would be aligned, while a small fraction of systems would exhibit a diverse range of stellar obliquities (e.g., Beaugé & Nesvorný 2012). With these predictions in mind, we aim to determine the dominant mechanisms responsible for shaping close-in planetary systems by characterizing

Corresponding author: Jiayin Dong  
jdong@flatironinstitute.org

\* Flatiron Research Fellow

the stellar obliquity distribution of exoplanetary systems through a Bayesian approach.

In exoplanetary observation, only the sky-projected stellar obliquity  $\lambda$ , the angle between the projections of  $\mathbf{n}_{\text{orb}}$  and  $\mathbf{n}_\star$  onto the plane of the sky, can be measured. This measurement is primarily obtained via the Rossiter-McLaughlin effect (Rossiter 1924; McLaughlin 1924). The stellar obliquity  $\psi$  can be determined, if both the sky-projected stellar obliquity  $\lambda$  and the stellar inclination  $i_\star$  are known. The relationship between  $\psi$  and  $\{\lambda, i_\star\}$  is given by (e.g., Fabrycky & Winn 2009):

$$\cos \psi = \sin i_\star \sin i_{\text{orb}} \cos \lambda + \cos i_\star \cos i_{\text{orb}}, \quad (1)$$

where  $i_{\text{orb}}$  is the inclination angle between the vector  $\mathbf{n}_{\text{orb}}$  and the observer's line of sight, and  $i_\star$  is the inclination angle between  $\mathbf{n}_\star$  and the observer's line of sight. In transiting-exoplanet systems where  $i_{\text{orb}} \approx 90^\circ$ ,  $\cos \psi \approx \sin i_\star \cos \lambda$ .

Stellar inclinations can often be constrained via, e.g., photometric and spectroscopic rotational modulation introduced by starspots for cool stars (e.g., Masuda & Winn 2020; Albrecht et al. 2021), gravity darkening for fast-rotating stars (e.g., Barnes 2009; Barnes et al. 2011), and asteroseismology for bright stars (e.g. Chaplin et al. 2013). For systems without  $i_\star$  measurements, it is still possible to infer their stellar obliquities from the sky-projected obliquities, assuming isotropic stellar inclinations; however, the inferred  $\psi$  will have greater uncertainty than the one inferred with  $i_\star$  measurement (Fabrycky & Winn 2009).

The relationship between the distributions of stellar obliquity, sky-projected stellar obliquity, and stellar inclination is still not fully understood. In this study, we aim to gain a deeper understanding of this relationship and develop a statistical approach to infer the stellar obliquity distribution. In Section 2, we introduce a flexible, hierarchical Bayesian framework that allows us to infer the stellar obliquity distribution of a sample. In Section 3, we apply the framework to simulated data and real observations and show that the inferred stellar obliquity distribution from sky-projected stellar obliquities is robust even if the  $i_\star$  information is not provided. In Section 4, we further investigate the relationship between the distributions of  $\psi$ ,  $\lambda$ , and  $i_\star$ , and explain why sky-projected stellar obliquities play a predominant role in determining the inferred distribution of stellar obliquities.

## 2. HIERARCHICAL BAYESIAN FRAMEWORK

To find the stellar obliquity distribution of exoplanetary systems, we develop a hierarchical Bayesian framework that takes the observed sky-projected stellar obliquity  $\lambda$  and orbital inclination  $i_{\text{orb}}$  as input data. The

measurement of the stellar inclination  $i_\star$  is optional. In the absence of  $i_\star$  information, we assume that it follows an isotropic distribution. Otherwise, the observed  $i_\star$  can be taken from previous measurements, or if the rotational modulation method is employed, the  $i_\star$  value can be inferred from the stellar rotation period  $P_{\text{rot}}$ , stellar radius  $R_\star$ , and sky-projected rotational broadening velocity  $v \sin i_\star$ .

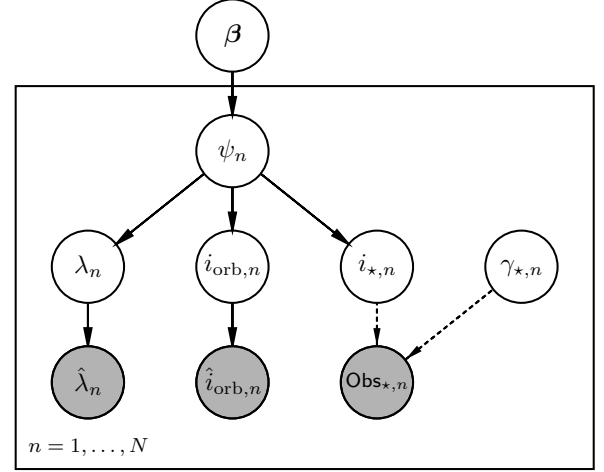


**Figure 1.** Hierarchical Bayesian framework to infer the stellar obliquity distribution of exoplanetary systems. The distribution is described by hyperparameters  $\beta$  and is constrained by the sky-projected stellar obliquity  $\lambda_n$ , orbital inclination  $i_{\text{orb},n}$ , and, if available, the stellar inclination  $i_{\star,n}$  of each  $n$ th individual system. The system's stellar obliquity  $\psi_n$  is calculated based on these parameters. Properties of the star other than its inclination, such as its radius and rotation period, are represented by  $\gamma_{\star,n}$ .  $\text{Obs}_{\star,n}$  contains all observed properties of the star with uncertainties,  $\hat{\lambda}_n$  has the measured sky-projected stellar obliquity and its uncertainty, and  $\hat{i}_{\text{orb},n}$  has measured orbital inclination and its uncertainty.

Figure 1 illustrates the probabilistic graphical model for our hierarchical Bayesian framework. We aim to constrain a set of hyperparameters  $\beta$  that describes the stellar obliquity distribution. The parameter set  $\beta$  is constrained by  $N$  individual systems, where each  $\psi_n$  is computed from the system's sky-projected stellar obliquity  $\lambda_n$ , the orbital inclination  $i_{\text{orb},n}$ , and if available, the stellar inclination  $i_{\star,n}$ . The parameter  $\gamma_{\star,n}$  contains all stellar properties other than  $i_{\star,n}$ , such as the stellar rotation period  $P_{\text{rot},n}$ , radius  $R_{\star,n}$ , and projected rotational velocity  $v \sin i_{\star,n}$ , if they are known.

The sky-projected stellar obliquity  $\lambda_n$  is constrained by observed  $\hat{\lambda}_n$  via the Rossiter-McLaughlin effect or gravity darkening. The orbital inclination  $i_{\text{orb},n}$  of exo-

planets is inferred from their transit light curves.  $\text{Obs}_{\star,n}$  includes observed data that helps to constrain  $i_{\star,n}$  and  $\gamma_{\star,n}$ . If the rotational modulation method is used to constrain the stellar inclination, the  $i_{\star,n}$  and  $\gamma_{\star,n}$  are constrained by rotational modulation in photometric or spectroscopic time series and observed sky-projected stellar rotational line broadening  $\hat{v} \sin i_{\star,n}$  (e.g., [Masuda & Winn 2020](#)), where we have  $v \sin i_{\star} = 2\pi R_{\star}/P_{\text{rot}}$ . If the gravity-darkening method is used, the  $i_{\star,n}$  could be constrained by the anomaly in transit light curves ([Barnes 2009](#)). If asteroseismology is used, the  $i_{\star,n}$  could be constrained from the mode splitting in the Fourier transform of photometric time series ([Chaplin et al. 2013](#)).

For the stellar obliquity distribution, we model the  $\cos \psi$  distribution instead of  $\psi$  distribution to understand if the stellar obliquity is isotropically distributed. If stellar obliquity distribution follows an isotropic distribution, the  $\cos \psi$  distribution will be uniformly distributed between -1 to 1. We adopt a two-component mixture Beta distribution with hyperparameters  $\beta = \{\mathbf{w}, \mathbf{a}, \mathbf{b}\}$ , where each hyperparameter has a dimension of 2. One component is designed for a large population of well-aligned systems, and the other is designed for misaligned systems. The Beta distribution is a flexible distribution that can describe the spike of aligned systems with stellar obliquities close to  $0^\circ$  or the clustered or broadly distributed misaligned systems. The probability density function of  $\cos \psi$  follows

$$\cos \psi \sim 2 \times \left( w_0 \text{Beta}(a_0, b_0) + w_1 \text{Beta}(a_1, b_1) \right) - 1. \quad (2)$$

Since the Beta distribution is defined on the interval  $[0, 1]$ , we extend its support to  $[-1, 1]$  using a linear transformation (i.e.,  $2 \times \text{Beta} - 1$ ). For the  $\text{Beta}(a_0, b_0)$  component, we have it to describe the population of aligned systems. For the  $a_0/b_0 \gg 1$ , the distribution will have a spike at  $\cos \psi = 1$ . For the  $\text{Beta}(a_1, b_1)$  component, we have it to describe the misaligned systems. We design the order of the two components to prevent label switching in the mixture model. With the design, the hyperparameter and parameter priors are the fol-


lowing:

$$\begin{aligned} w_{0,1} &\sim \text{Dirichlet}(1, 1) \\ a_0 &\sim \mathcal{U}(0, 50) \\ b_0 &\sim \mathcal{U}(0, 1) \\ a_1 &\sim \mathcal{U}(0, 10) \\ b_1 &\sim \mathcal{U}(0, 10) \\ \cos i_{\star,n} &\sim \mathcal{U}(0, 1) \\ \cos i_{\text{orb},n} &\sim \mathcal{U}(-1, 1) \\ \lambda_{\star,n} &\sim \mathcal{U}(0, \pi). \end{aligned} \quad (3)$$

The likelihood functions follow:

$$\begin{aligned} \mathcal{L}(\lambda) &\sim \prod_{i=1}^N \mathcal{N}(\hat{\lambda}_n, \sigma_{\hat{\lambda}_n}) \\ \mathcal{L}(i_{\text{orb}}) &\sim \prod_{i=1}^N \mathcal{N}(\hat{i}_{\text{orb},n}, \sigma_{\hat{i}_{\text{orb},n}}) \\ \mathcal{L}(i_{\star}) &\sim \prod_{i=1}^N \mathcal{N}(\text{Obs}_{\star,n}, \sigma_{\text{Obs}_{\star,n}}). \end{aligned} \quad (4)$$

If  $\gamma_{\star,n}$  is available, we construct Normal distributions with means and standard deviations from measurements. Here we use uniform hyperpriors for the Beta distribution. However, it is important to note that when applying the framework to a small sample size with  $N \lesssim 50$ , the choice of hyperpriors could impact the inferred distribution ([Nagpal et al. 2022](#)). To ensure the robustness of the inferred distributions in such cases, it is crucial to test their sensitivity to different hyperpriors.

The probabilistic model is constructed using the PyMC package version v4.1.7 ([Wiecki et al. 2022](#)), and the posteriors are sampled with the No-U-Turn Sampler (NUTS; [Hoffman & Gelman 2011](#)), which is a gradient-based Markov chain Monte Carlo (MCMC) sampling algorithm. This paper's figures and simulations are completely reproducible and were created using the **show your work!** package. The open-source code is available on GitHub  (<https://github.com/jiayindong/obliquity>).

### 3. APPLICATIONS TO SIMULATED AND OBSERVED DATA

#### 3.1. Simulated Data

We first apply the hierarchical Bayesian framework to simulated data of which the ground-truth stellar obliquity distribution is known. We test the four  $\cos \psi$  distributions: a uniform distribution  $\mathcal{U}(-1, 1)$  and three Normal distributions  $\mathcal{N}(0, 0.2)$ ,  $\mathcal{N}(-0.4, 0.2)$ , and  $\mathcal{N}(0.4, 0.2)$ . For each  $\cos \psi$  distribution, we randomly

generate 200 samples of stellar inclination  $i_*$  and sky-projected stellar obliquity  $\lambda$ . We assume the stellar spin axis is uniformly distributed around the planetary orbital axis in the azimuthal direction and the orbital inclination is  $90^\circ$ . The sampled  $i_*$  and  $\lambda$  here are *true* values. We then add some Gaussian noises to the *true*  $\lambda$  and  $i_*$  to simulate the *observed* data. We choose uncertainties of  $\sigma_\lambda = 8^\circ$  and  $\sigma_{i_*} = 10^\circ$ , which are typical observational uncertainties summarized in [Albrecht et al. \(2022\)](#). Using the observed  $\lambda$  and their uncertainties, we infer the  $\cos\psi$  distribution of the sample with or without  $i_*$  likelihoods.

In Figure 2, we present the inferred stellar obliquity distributions. Since the simulated stellar obliquity distributions only have a single component, we model the data with a single Beta distribution. Each row of Figure 2 corresponds to an injected stellar obliquity distribution. The orange curve and contours are the median and  $1\text{-}\sigma$  and  $2\text{-}\sigma$  uncertainties of the inferred  $\cos\psi$  distribution with stellar inclination information, and the blue curve and contours are the ones without stellar inclination information. We simply assume an isotropic distribution of  $i_*$  for these models. Surprisingly, as shown in Figure 2, the inferred distributions of  $\cos\psi$ , whether or not they include the information of  $i_*$ , correctly recover the injected distributions (represented by grey dashed lines) in all four cases. Despite the fact that the inferred distributions without  $i_*$  measurements may have wider uncertainties, as indicated by shallow color contours, the modes and widths of the inferred stellar obliquity distributions are consistent with or without  $i_*$  likelihood. Since the injected distributions in rows 2-4 are Normal distributions, it should not be surprising that the inferred distributions, which are Beta distributions, may not exactly match the injected distributions.

We also examine the role of orbital inclination  $i_{\text{orb}}$  in the stellar obliquity distribution inference. Since our study focuses on transiting-exoplanet systems, we consider an isotropic orbital inclination distribution between  $80^\circ$  and  $90^\circ$ . This broad range of inclinations corresponds to an impact parameter range from 0 to 1 with a planet-star separation  $a/R_*$  of 6. We compare the stellar obliquity distributions obtained by approximating  $i_{\text{orb}}$  to  $90^\circ$  with the distributions obtained using the actual  $i_{\text{orb}}$ . We find the difference between the two distributions is negligible. This suggests that for transiting-exoplanet systems, approximating orbital inclinations as  $90^\circ$  will not compromise the stellar obliquity distribution inference.

We demonstrate through simulations that the inferred stellar obliquity distribution is robust even if the  $i_*$  information is not provided, and the  $i_*$  measurement only

improves the constraint on the stellar obliquity distribution. Later in Section 4, we derive the Jacobian transformations between  $\psi$ ,  $\lambda$ , and  $i_*$  to understand why sky-projected stellar obliquities play a predominant role in determining the inferred distribution of stellar obliquities.

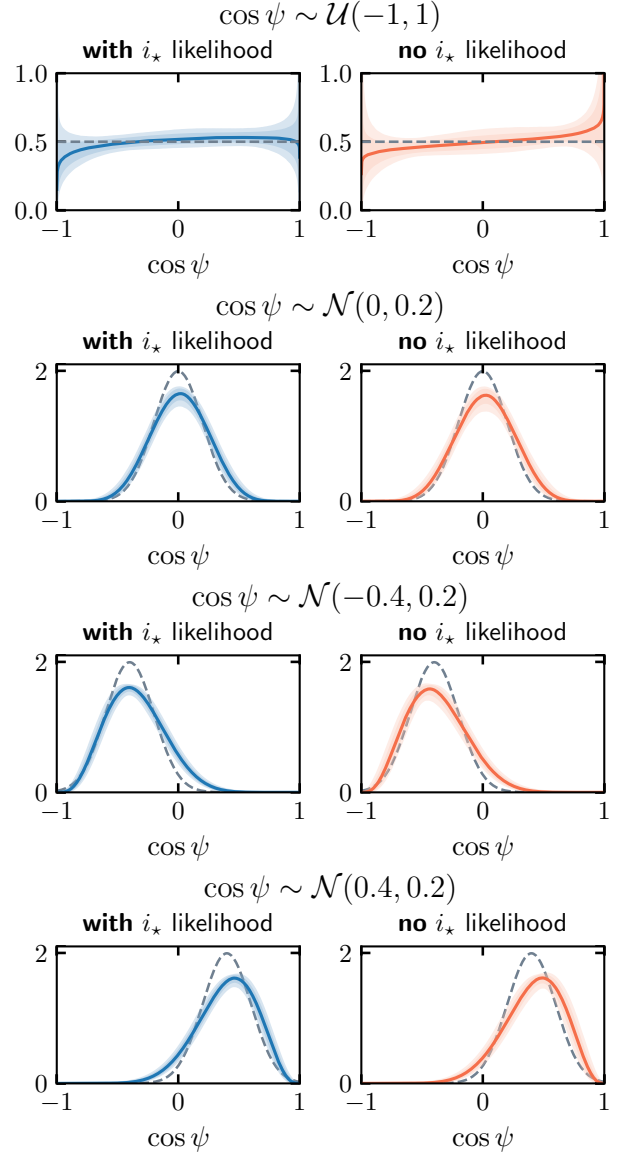


**Figure 2.** Inferred stellar obliquity distributions from sky-projected stellar obliquities with and without information on the stellar inclination, depicted in blue and orange curves, respectively. Each row presents a set of simulated data with the true distribution of  $\cos\psi$  indicated by grey dashed curves. The shallow contours represent the  $1\text{-}\sigma$  and  $2\text{-}\sigma$  uncertainties of the inferred distributions.

### 3.2. Exoplanetary Stellar Obliquity Distribution

We next apply our hierarchical Bayesian framework to a sample of 161 exoplanetary systems with sky-projected stellar obliquity measurements, primarily consisting of Hot Jupiter systems, as summarized in [Albrecht et al. \(2022\)](#) Table A1. The inferred  $\cos \psi$  distribution is shown in Figure 3. The  $\cos \psi$  distribution is peaked at 1, with nearly flat behavior between  $-0.75$  and  $0.75$  and no significant clustering. The distribution suggests that there is a pile-up of planetary systems with stellar obliquities less than  $40^\circ$  and an isotropic distribution for obliquities between  $40^\circ$  and  $140^\circ$ . The fraction of aligned systems dominates the distribution, with  $w_0 = 0.67 \pm 0.09$ . The corresponding hyperposteriors of the Beta distribution are  $a_0 = 31.0 \pm 12.8$  and  $b_0 = 0.40 \pm 0.12$ . On the other hand, the fraction of misaligned systems is estimated to be  $w_1 = 0.33 \pm 0.09$ , with hyperposteriors of  $a_1 = 1.56 \pm 0.93$  and  $b_1 = 1.64 \pm 1.58$ .

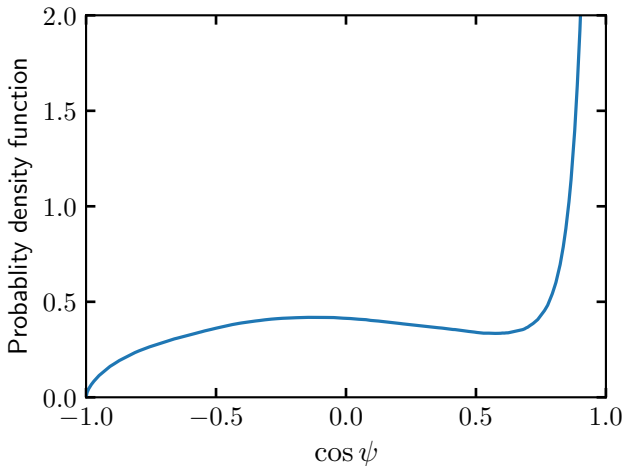


**Figure 3.** Inferred stellar obliquity distribution for all exoplanetary systems with sky-projected stellar obliquity measurements. This inference is based purely on the observed sky-projected obliquities and assumes an isotropic distribution for the stellar inclinations.

The discrepancy between the inferred stellar obliquity distribution of the full sample of exoplanetary systems and the previous analysis of the subsample with  $i_*$  measurements warrants further investigation. The earlier study identified a preponderance of perpendicular planets and disfavored an isotropic stellar obliquity distribution ([Albrecht et al. 2021](#)). There are two potential explanations for this difference: (1) the subsample with  $i_*$  measurements is small and only includes about 20 misaligned systems, and (2) the requirement for  $i_*$  measurements could introduce selection biases in the sample.

The inferred stellar obliquity distribution indicates that approximately  $67 \pm 9\%$  of the systems have a stellar

obliquity of less than  $40^\circ$ , and approximately  $33 \pm 9\%$  of the systems follow a nearly isotropic stellar obliquity distribution ranging from  $\sim 40^\circ$  to  $\sim 140^\circ$ . These findings could have significant implications for the formation and evolution of close-in planetary systems. The broad distribution of misaligned systems is in good agreement with the predicted outcome of multiple giant planets scattering after a convergent disk migration, as proposed by various studies, such as [Nagasawa & Ida \(2011\)](#) and [Beaugé & Nesvorný \(2012\)](#). The intriguing result should be further examined with a more carefully selected sample of Hot Jupiters and provides opportunities to place constraints on their origin channels of Hot Jupiters.

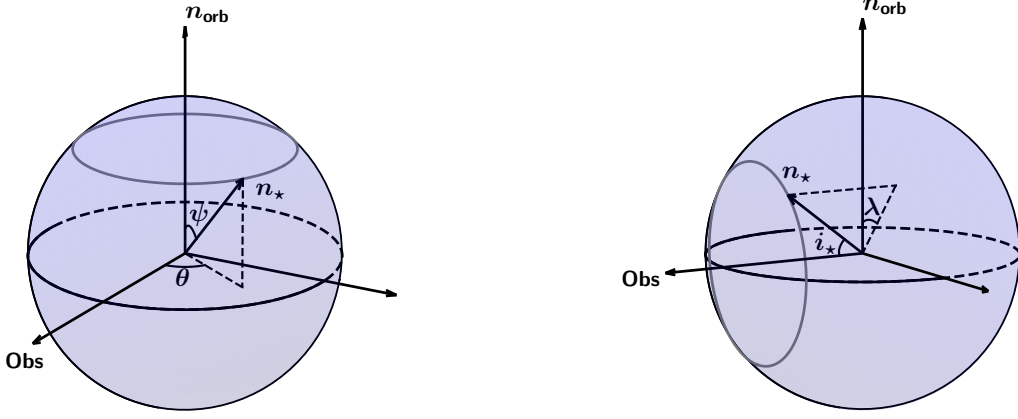
#### 4. RELATIONS BETWEEN THE $\psi$ , $\lambda$ , AND $i_*$ DISTRIBUTIONS

In this section, we aim to gain insight into the reasons behind the predominant role of the sky-projected stellar obliquity distribution and the less significant impact of the stellar inclination distribution in the inference of the stellar obliquity distribution.

In Figure 4, we present two coordinate systems that describe the stellar spin axis  $\mathbf{n}_*$  for a given orbital axis  $\mathbf{n}_{\text{orb}}$ . In both coordinates, we set the observer's line of sight to be one of the horizontal axes (represented as the conventional  $x$ -axis in Cartesian coordinates), and the orbital axis of the planet to be the vertical axis (represented as the conventional  $z$ -axis in Cartesian coordinates). To simplify the problem, the orbital inclination of the transiting planet is assumed to be  $90^\circ$  in this illustration. As discussed in Section 3.1, the assumption will not compromise the stellar obliquity distribution inference for transiting planets.

The  $\{\psi, \theta\}$  coordinate system shown in panel (a) relates to the physical properties of a planetary system.  $\psi$  is the angle between the stellar spin axis and the planetary orbital axis, and  $\theta$  is the azimuthal angle of the stellar spin axis. For the given  $\mathbf{n}_{\text{orb}}$  axis, if  $\mathbf{n}_*$  is a random vector with uniform distribution on a three-dimensional sphere, i.e.,  $\mathbf{n}_*$  is isotropically distributed, the probability density function of  $\psi$  follows  $p_\psi \sim \sin \psi$  and  $p_\theta \sim 1/2\pi$ . Since  $p_{\cos \psi} = p_\psi |d\psi/d\cos \psi|$ ,  $p_{\cos \psi}$  is uniformly distributed between  $-1$  and  $1$  for isotropic stellar obliquity. The  $\{\lambda, i_*\}$  coordinate system shown in panel (b) relates to observed properties.  $\lambda$  is the sky-projected stellar obliquity and  $i_*$  is the stellar inclination. If  $\mathbf{n}_*$  is isotropically distributed,  $p_{i_*} \sim \sin i_*$  and  $p_\lambda \sim \mathcal{U}(-\pi, \pi)$ . Again, since  $p_{\cos i_*} = p_{i_*} |di_*/d\cos i_*|$ ,  $p_{\cos i_*}$  is uniformly distributed between  $-1$  and  $1$ . Because of the observational degeneracy between  $i_*$  and  $180^\circ - i_*$ , the convention is to have  $0 \leq i_* \leq 90^\circ$ , and





(a) The  $\{\psi, \theta\}$  coordinate system. The grey circle corresponds to a constant  $\psi$  value and its circumference is proportional to  $\sin \psi$ .

(b) The  $\{\lambda, i_\star\}$  coordinate system. The grey circle corresponds to a constant  $i_\star$  value and its circumference is proportional to  $\sin i_\star$ .

**Figure 4.** Two coordinate systems that describe the stellar spin axis  $\mathbf{n}_\star$  and the planet's orbital axis  $\mathbf{n}_{\text{orb}}$ . Here we define the observer's line of sight as one of the horizontal axes (represented as the conventional  $x$ -axis in Cartesian coordinates), and the orbital axis of the planet as the vertical axis (represented as the conventional  $z$ -axis in Cartesian coordinates). We approximate the orbital inclination of the planet to  $90^\circ$ .

thus  $p_{\cos i_\star}$  is uniformly distributed between 0 and 1 and  $p_{\cos i_\star} \sim \mathcal{U}(0, 1)$ . This also limits  $p_\theta \sim \mathcal{U}(-\pi/2, \pi/2)$ .

We could find the mathematical relations between  $\{\psi, \theta\}$  and  $\{\lambda, i_\star\}$  by pairing the Cartesian components of  $\mathbf{n}_\star$  in two coordinate systems:

$$\sin \psi \cos \theta = \cos i_\star \quad (5)$$

$$\sin \psi \sin \theta = \sin \lambda \sin i_\star \quad (6)$$

$$\cos \psi = \cos \lambda \sin i_\star. \quad (7)$$

First, we derive the  $\lambda$  distribution for a given  $\cos \psi$  distribution. We could find the distribution of  $\cos \lambda$  using the Jacobian transformation from  $\cos \psi$  and  $\cos \theta$ . Since  $\psi$  and  $\theta$  are independent variables, we could marginalize over  $\theta$  to find the relation between the probability density functions between  $\lambda$  and  $\psi$ . The Jacobian transformation follows

$$p_{\cos \lambda} = \int \left| \frac{\partial \cos \psi}{\partial \cos \lambda} \right| p_{\cos \psi} p_{\cos \theta} d \cos \theta. \quad (8)$$

Replacing  $\sin i_\star$  in Equation (7) using Equation (5), we find  $\cos \lambda = \cos \psi / \sqrt{1 - (1 - \cos^2 \psi) \cos^2 \theta}$ . Reorganize the equation, we get  $\cos^2 \psi = \frac{\cos^2 \lambda \cos^2 \theta - \cos^2 \lambda}{\cos^2 \lambda \cos^2 \theta - 1}$  and the partial derivative  $\left| \frac{\partial \cos \psi}{\partial \cos \lambda} \right| = \frac{(1 - \cos^2 \theta)^{1/2}}{(1 - \cos^2 \theta \cos^2 \lambda)^{3/2}}$ . Assume  $\theta$  is uniformly distributed between  $-\pi/2$  and  $\pi/2$ ,  $p_{\cos \theta} = p_\theta |d\theta/d \cos \theta| = 2/\pi / (1 - \cos^2 \theta)^{1/2}$ , where the factor of 2 is due to two solutions of  $\theta$  to the  $\cos \theta$ . Putting all the parts together, we get

$$p_{\cos \lambda} = \frac{2}{\pi} \int_0^1 (1 - \cos^2 \theta \cos^2 \lambda)^{-3/2} p_{\cos \psi} d \cos \theta. \quad (9)$$

If  $\cos \psi$  is uniformly distribution, i.e.,  $p_{\cos \psi} \sim 1/2$ , Equation (9) becomes  $p_{\cos \lambda} \sim 1/\pi / \sqrt{1 - \cos^2 \lambda}$ , which is equivalent to  $p_\lambda \sim \mathcal{U}(-\pi, \pi)$ . This suggests  $\lambda$  is uniformly distributed for an isotropic  $\psi$  distribution. For different  $\cos \psi$  distributions,  $p_\lambda$  can be found by evaluating Equation (9).

Next, we derive the  $i_\star$  distribution for a given  $\cos \psi$  distribution. Similarly, we first find the Jacobian transformation of  $i_\star$  from  $\psi$  and  $\theta$  and then marginalize over  $\theta$ . It is easier to work on  $\cos i_\star$  than  $i_\star$ :

$$p_{\cos i_\star} = \int \left| \frac{\partial \sin \psi}{\partial \cos i_\star} \right| p_{\sin \psi} p_{\cos \theta} d \cos \theta. \quad (10)$$

From Equation (5), we have  $\sin \psi = \cos i_\star / \cos \theta$  and  $\left| \frac{\partial \sin \psi}{\partial \cos i_\star} \right| = 1/\cos \theta$ . Again, we assume  $\theta$  is uniformly distributed, and this gives  $p_{\cos \theta} = 2/\pi / (1 - \cos^2 \theta)^{1/2}$ . Lastly, we transform the  $p_{\sin \psi}$  to  $p_{\cos \psi}$ , where  $p_{\sin \psi} = 2p_{\cos \psi} \sin \psi / \sqrt{1 - \sin^2 \psi}$  and the factor of 2 is from two solutions of  $\cos \psi$  to the  $\cos^2 \psi = 1 - \sin^2 \psi$ . Combining all the pieces together, we get

$$p_{\cos i_\star} = \frac{4}{\pi} \int_{\cos i_\star}^1 \frac{\cos i_\star / \cos \theta}{\sqrt{\cos^2 \theta - \cos^2 i_\star}} \frac{1}{\sqrt{1 - \cos^2 \theta}} p_{\cos \psi} d \cos \theta. \quad (11)$$

Note that the lower limit of the integral is  $\cos i_\star$  instead of 0 since  $|\cos \theta / \cos i_\star| \geq 1$ . If  $\cos \psi$  is uniformly distribution, i.e.,  $p_{\cos \psi} \sim 1/2$ , the integral gives 1, which suggests the  $\cos i_\star$  is uniformly distributed, as expected.

Using Equation (9) and (11), we can now derive the  $\lambda$  and  $i_\star$  distributions for any given  $\psi$  distributions, as-

suming the azimuthal angle of the stellar spin axis  $\theta$  is random. In Figure 5, we present numerical solutions of the  $\lambda$  and  $i_*$  distributions for four different  $\cos\psi$  distributions. The top row of Figure 5 shows an isotropic  $\psi$  distribution, where  $\cos\psi \sim \mathcal{U}(-1, 1)$ . The second, third, and fourth rows of Figure 5 present Normal distributions of  $\cos\psi$  following  $\mathcal{N}(0, 0.2)$ ,  $\mathcal{N}(-0.4, 0.2)$ , and  $\mathcal{N}(0.4, 0.2)$ , respectively. The blue curves in each row show the numerical solutions of the  $\lambda$  and  $i_*$  distributions, while the grey histograms show the sampling of  $\lambda$  and  $i_*$  from the  $\cos\psi$  and  $\theta$  distributions. For a uniform  $\cos\psi$  distribution, the  $\lambda$  distribution is uniform, and the  $i_*$  distribution is isotropic, proportional to  $\sin i_*$ , as expected.

Interestingly, the  $\lambda$  distribution is closely related to and sensitive to the underlying  $\psi$  distribution, as demonstrated in the 1<sup>st</sup> and 2<sup>nd</sup> columns in Figure 5. For different stellar obliquities, the  $\lambda$  distributions are distinguishable, making it possible to infer the  $\psi$  distribution from the  $\lambda$  distribution. On the other hand, the  $i_*$  distributions are less dependent on the underlying  $\psi$  distribution. Compared to an isotropic  $i_*$  distribution, the curvature of the  $i_*$  distributions for different  $\psi$  distributions differ the most at the low  $i_*$  values (i.e.,  $i_* < \pi/4$ ), which places a challenge to observational detections. Additionally, the degeneracy of the solution could be a significant issue when attempting to infer the  $\psi$  distribution from the  $i_*$  distribution. For example, when  $\cos\psi \sim \mathcal{N}(-0.4, 0.2)$  or  $\cos\psi \sim \mathcal{N}(0.4, 0.2)$ , two  $i_*$  distributions are exactly the same.

The  $\psi$  distribution can be inferred from the  $\lambda$  distribution without loss of information due to the strong dependency of the  $\lambda$  distribution on the  $\psi$  distribution. It is also worthwhile to note that although we could find a mathematical expression of  $\psi$  with  $\lambda$  and  $\theta$ , the  $\psi$  distribution cannot be inferred from the two variables since they are not independent variables.

In the 4<sup>th</sup> column in Figure 5, the  $\psi$  distribution is found from the  $\lambda$  distribution by assuming an isotropic  $i_*$  distribution. The method could accurately recover the peaks and widths of the underlying  $\psi$  distributions (represented by blue dashed lines) shown in grey histograms. The method over-predicts  $\cos\psi$  at  $\pm 1$  because of the over-prediction of  $i_*$  near  $90^\circ$ . However, this small deviation from the true distribution has a limited impact on population inference because of the hyperparameters have limited degrees of freedom. By comparing the blue curves with the orange curves in Figure 2, it can be seen that the overestimation of  $\cos\psi$  near  $\pm 1$  under the assumption of isotropic  $i_*$  has little effect on the overall inference. The distribution is primarily determined by the peak and width of the stellar obliquity distribution,

both of which are correctly predicted by the isotropic  $i_*$  model.

## 5. SUMMARY & DISCUSSION

In this work, we demonstrated that the stellar obliquity distribution could be robustly inferred from sky-projected stellar obliquities purely. We introduced a flexible, hierarchical Bayesian framework for the stellar obliquity distribution inference. Stellar inclination measurements are optional input in the model, and if not available, they are assumed to be isotropically distributed. Our open-source hierarchical Bayesian model, available on GitHub [🔗](https://github.com/jiayindong/obliquity) (<https://github.com/jiayindong/obliquity>), can be customized to different stellar obliquity distributions and priors for specific target samples.

It is crucial to consider the representativeness of the  $i_*$  sample when jointly modeling the stellar obliquity distribution from two data sets, one with and one without  $i_*$  measurements. An unrepresentative  $i_*$  sample could tighten the constraints on the stellar obliquities and bias the interpretation of the overall distribution.

Finally, we applied the framework to all exoplanetary systems to all exoplanetary systems with available sky-projected stellar obliquities and found that approximately  $67 \pm 9\%$  of the systems have a stellar obliquity less than  $40^\circ$ , and approximately  $33 \pm 9\%$  of the systems follow a nearly isotropic stellar obliquity distribution between  $\sim 40^\circ$  and  $\sim 140^\circ$ . The distribution could have important implications for the formation and evolution of close-in planetary systems and is worth further investigation.

This study was conducted using the **show your work!** reproducible workflow (Luger et al. 2021), which leverages continuous integration to automate the data retrieval from [zenodo.org](https://zenodo.org), figure generation, and manuscript compilation. The script used to produce each figure can be accessed via a link in the corresponding figure caption, as it corresponds to the latest build of the manuscript. The git repository for this study, which includes the Jupyter notebook demonstration and case studies of the stellar obliquity distribution inference, is publicly accessible at <https://github.com/jiayindong/obliquity>.

**Software:** ArviZ (Kumar et al. 2019), Jupyter (Kluyver et al. 2016), Matplotlib (Hunter 2007; Droetto et al. 2016), NumPy (van der Walt et al. 2011; Harris et al. 2020), pandas (Wes McKinney 2010; pandas development team 2020), PyMC (Wiecki et al. 2022), SciPy (Virtanen et al. 2020), **show your work!** (Luger et al. 2021)

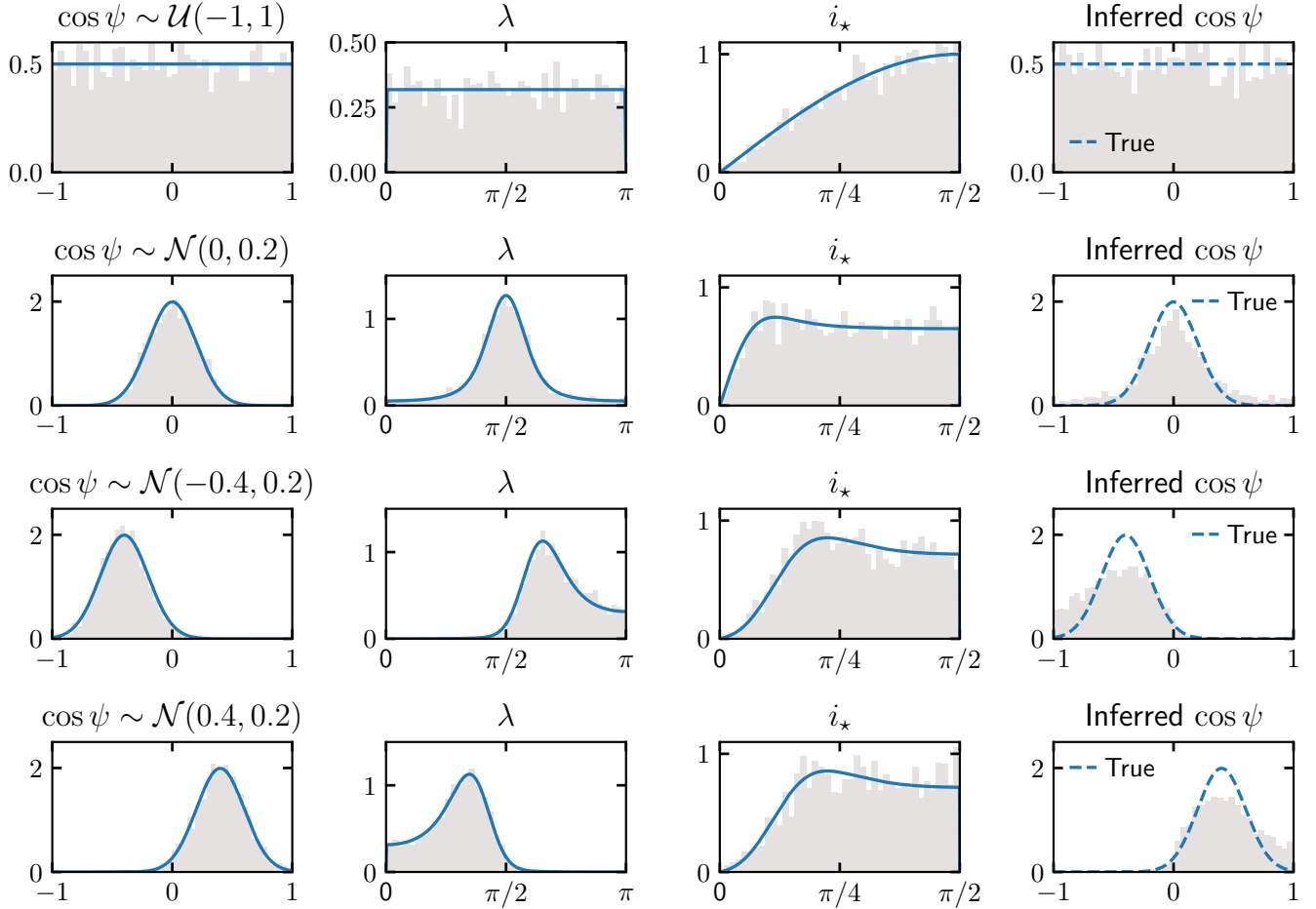


**Figure 5.** Simulated  $\cos \psi$  distributions (1<sup>st</sup> column) and the corresponding distributions of sky-projected stellar obliquity  $\lambda$  (2<sup>nd</sup> column) and stellar inclination  $i_*$  (3<sup>rd</sup> column). The inferred  $\cos \psi$  distributions assuming isotropic stellar inclinations are shown in the 4<sup>th</sup> column. The grey histograms present the random samplings of  $\lambda$  and  $i_*$  from the  $\cos \psi$  distributions, and the blue curves present the numerical solutions.

## REFERENCES

- Albrecht, S., Winn, J. N., Johnson, J. A., et al. 2012, *ApJ*, 757, 18, doi: [10.1088/0004-637X/757/1/18](https://doi.org/10.1088/0004-637X/757/1/18)
- Albrecht, S. H., Dawson, R. I., & Winn, J. N. 2022, *PASP*, 134, 082001, doi: [10.1088/1538-3873/ac6c09](https://doi.org/10.1088/1538-3873/ac6c09)
- Albrecht, S. H., Marcussen, M. L., Winn, J. N., Dawson, R. I., & Knudstrup, E. 2021, *ApJL*, 916, L1, doi: [10.3847/2041-8213/ac0f03](https://doi.org/10.3847/2041-8213/ac0f03)
- Anderson, K. R., Storch, N. I., & Lai, D. 2016, *MNRAS*, 456, 3671, doi: [10.1093/mnras/stv2906](https://doi.org/10.1093/mnras/stv2906)
- Barnes, J. W. 2009, *ApJ*, 705, 683, doi: [10.1088/0004-637X/705/1/683](https://doi.org/10.1088/0004-637X/705/1/683)
- Barnes, J. W., Linscott, E., & Shporer, A. 2011, *ApJS*, 197, 10, doi: [10.1088/0067-0049/197/1/10](https://doi.org/10.1088/0067-0049/197/1/10)
- Bate, M. R., Lodato, G., & Pringle, J. E. 2010, *MNRAS*, 401, 1505, doi: [10.1111/j.1365-2966.2009.15773.x](https://doi.org/10.1111/j.1365-2966.2009.15773.x)
- Batygin, K. 2012, *Nature*, 491, 418, doi: [10.1038/nature11560](https://doi.org/10.1038/nature11560)
- Beaugé, C., & Nesvorný, D. 2012, *ApJ*, 751, 119, doi: [10.1088/0004-637X/751/2/119](https://doi.org/10.1088/0004-637X/751/2/119)
- Chaplin, W. J., Sanchis-Ojeda, R., Campante, T. L., et al. 2013, *ApJ*, 766, 101, doi: [10.1088/0004-637X/766/2/101](https://doi.org/10.1088/0004-637X/766/2/101)
- Chatterjee, S., Ford, E. B., Matsumura, S., & Rasio, F. A. 2008, *ApJ*, 686, 580, doi: [10.1086/590227](https://doi.org/10.1086/590227)
- Droettboom, M., Hunter, J., Caswell, T. A., et al. 2016, *Matplotlib: Matplotlib V1.5.1*, v1.5.1, Zenodo, doi: [10.5281/zenodo.44579](https://doi.org/10.5281/zenodo.44579)
- Fabrycky, D., & Tremaine, S. 2007, *ApJ*, 669, 1298, doi: [10.1086/521702](https://doi.org/10.1086/521702)
- Fabrycky, D. C., & Winn, J. N. 2009, *ApJ*, 696, 1230, doi: [10.1088/0004-637X/696/2/1230](https://doi.org/10.1088/0004-637X/696/2/1230)



- Harris, C. R., Jarrod Millman, K., van der Walt, S. J., et al. 2020, arXiv e-prints, arXiv:2006.10256.  
<https://arxiv.org/abs/2006.10256>
- Hoffman, M. D., & Gelman, A. 2011, arXiv e-prints, arXiv:1111.4246. <https://arxiv.org/abs/1111.4246>
- Hunter, J. D. 2007, *Computing in Science and Engineering*, 9, 90, doi: [10.1109/MCSE.2007.55](https://doi.org/10.1109/MCSE.2007.55)
- Kluyver, T., Ragan-Kelley, B., Pérez, F., et al. 2016, in *Positioning and Power in Academic Publishing: Players, Agents and Agendas*, ed. F. Loizides & B. Schmidt (Netherlands: IOS Press), 87–90.  
<https://eprints.soton.ac.uk/403913/>
- Kumar, R., Carroll, C., Hartikainen, A., & Martin, O. 2019, *Journal of Open Source Software*, 4, 1143, doi: [10.21105/joss.01143](https://doi.org/10.21105/joss.01143)
- Lai, D., Foucart, F., & Lin, D. N. C. 2011, *MNRAS*, 412, 2790, doi: [10.1111/j.1365-2966.2010.18127.x](https://doi.org/10.1111/j.1365-2966.2010.18127.x)
- Luger, R., Bedell, M., Foreman-Mackey, D., et al. 2021, arXiv e-prints, arXiv:2110.06271.  
<https://arxiv.org/abs/2110.06271>
- Masuda, K., & Winn, J. N. 2020, *AJ*, 159, 81, doi: [10.3847/1538-3881/ab65be](https://doi.org/10.3847/1538-3881/ab65be)
- McLaughlin, D. B. 1924, *ApJ*, 60, 22, doi: [10.1086/142826](https://doi.org/10.1086/142826)
- Nagasawa, M., & Ida, S. 2011, *ApJ*, 742, 72, doi: [10.1088/0004-637X/742/2/72](https://doi.org/10.1088/0004-637X/742/2/72)
- Nagasawa, M., Ida, S., & Bessho, T. 2008, *ApJ*, 678, 498, doi: [10.1086/529369](https://doi.org/10.1086/529369)
- Nagpal, V., Blunt, S., Bowler, B. P., et al. 2022, arXiv e-prints, arXiv:2211.02121.  
<https://arxiv.org/abs/2211.02121>
- Naoz, S. 2016, *ARA&A*, 54, 441, doi: [10.1146/annurev-astro-081915-023315](https://doi.org/10.1146/annurev-astro-081915-023315)
- pandas development team, T. 2020, pandas-dev/pandas: Pandas, latest, Zenodo, doi: [10.5281/zenodo.3509134](https://doi.org/10.5281/zenodo.3509134)
- Rasio, F. A., & Ford, E. B. 1996, *Science*, 274, 954, doi: [10.1126/science.274.5289.954](https://doi.org/10.1126/science.274.5289.954)
- Rogers, T. M., Lin, D. N. C., & Lau, H. H. B. 2012, *ApJL*, 758, L6, doi: [10.1088/2041-8205/758/1/L6](https://doi.org/10.1088/2041-8205/758/1/L6)
- Rogers, T. M., Lin, D. N. C., McElwaine, J. N., & Lau, H. H. B. 2013, *ApJ*, 772, 21, doi: [10.1088/0004-637X/772/1/21](https://doi.org/10.1088/0004-637X/772/1/21)
- Rossiter, R. A. 1924, *ApJ*, 60, 15, doi: [10.1086/142825](https://doi.org/10.1086/142825)
- Teyssandier, J., Lai, D., & Vick, M. 2019, *MNRAS*, 486, 2265, doi: [10.1093/mnras/stz1011](https://doi.org/10.1093/mnras/stz1011)
- van der Walt, S., Colbert, S. C., & Varoquaux, G. 2011, *Computing in Science and Engineering*, 13, 22, doi: [10.1109/MCSE.2011.37](https://doi.org/10.1109/MCSE.2011.37)
- Vick, M., Lai, D., & Anderson, K. R. 2019, *MNRAS*, 484, 5645, doi: [10.1093/mnras/stz354](https://doi.org/10.1093/mnras/stz354)
- Virtanen, P., Gommers, R., Oliphant, T. E., et al. 2020, *Nature Methods*, 17, 261, doi: [10.1038/s41592-019-0686-2](https://doi.org/10.1038/s41592-019-0686-2)
- Wes McKinney. 2010, in *Proceedings of the 9th Python in Science Conference*, ed. Stéfan van der Walt & Jarrod Millman, 56 – 61, doi: [10.25080/Majora-92bf1922-00a](https://doi.org/10.25080/Majora-92bf1922-00a)
- Wiecki, T., Salvatier, J., Patil, A., et al. 2022, *pymc-devs/pymc*, v4.1.7, Zenodo, Zenodo, doi: [10.5281/zenodo.7467113](https://doi.org/10.5281/zenodo.7467113)
- Winn, J. N., Fabrycky, D., Albrecht, S., & Johnson, J. A. 2010, *ApJL*, 718, L145, doi: [10.1088/2041-8205/718/2/L145](https://doi.org/10.1088/2041-8205/718/2/L145)
- Wu, Y., & Lithwick, Y. 2011, *ApJ*, 735, 109, doi: [10.1088/0004-637X/735/2/109](https://doi.org/10.1088/0004-637X/735/2/109)
- Wu, Y., & Murray, N. 2003, *ApJ*, 589, 605, doi: [10.1086/374598](https://doi.org/10.1086/374598)